Simulation of ultrasonic pulse propagation, distortion, and attenuation in the human chest wall

T. Douglas Mast
Applied Research Laboratory, The Pennsylvania State University, University Park, Pennsylvania 16802

Laura M. Hinkelman[a)]
Department of Electrical and Computer Engineering, University of Rochester, Rochester, New York 14627

Leon A. Metlay
Department of Pathology and Laboratory Medicine, University of Rochester Medical School, Rochester, New York 14642

Michael J. Orr
Department of Electrical and Computer Engineering, University of Rochester, Rochester, New York 14627

Robert C. Waag
Departments of Electrical and Computer Engineering and Radiology, University of Rochester, Rochester, New York 14627

(Received 5 April 1999; accepted for publication 23 August 1999)

A finite-difference time-domain model for ultrasonic pulse propagation through soft tissue has been extended to incorporate absorption effects as well as longitudinal-wave propagation in cartilage and bone. This extended model has been used to simulate ultrasonic propagation through anatomically detailed representations of chest wall structure. The inhomogeneous chest wall tissue is represented by two-dimensional maps determined by staining chest wall cross sections to distinguish between tissue types, digitally scanning the stained cross sections, and mapping each pixel of the scanned images to fat, muscle, connective tissue, cartilage, or bone. Each pixel of the tissue map is then assigned a sound speed, density, and absorption value determined from published measurements and assumed to be representative of the local tissue type. Computational results for energy level fluctuations and arrival time fluctuations show qualitative agreement with measurements performed on the same specimens, but show significantly less waveform distortion than measurements. Visualization of simulated tissue–ultrasound interactions in the chest wall shows possible mechanisms for image aberration in echocardiography, including effects associated with reflection and diffraction caused by rib structures. A comparison of distortion effects for varying pulse center frequencies shows that, for soft tissue paths through the chest wall, energy level and waveform distortion increase markedly with rising ultrasonic frequency and that arrival-time fluctuations increase to a lesser degree. [S0001-4966(99)03212-9]

PACS numbers: 43.80.Qf, 43.80.Cs, 43.58.Ta, 43.20.Fn [FD]

INTRODUCTION

Echocardiography is widely employed for diagnosis of cardiac diseases including valvular defects, pericardial effusion, and wall motion abnormalities.[1–3] Commonly, echocardiography is performed noninvasively through the chest (transthoracic) using an external probe placed on the chest wall. The chest wall, however, can considerably degrade image quality because acoustic paths between the skin and heart may contain ribs and cartilage as well as inhomogeneous muscle and fatty tissue. The result is that as many as 10–30% of patients cannot be successfully imaged with present transthoracic techniques.[4] This limitation of transthoracic echocardiography has led to the development of transesophageal echocardiography, in which the heart is imaged by a transducer inserted into the esophagus.[1–4] Although transesophageal echocardiography provides superior image quality, resulting in high diagnostic sensitivity and specificity, the invasiveness of the procedure is accompanied by increased risk.[3–6] For this reason, improvements in the noninvasive transthoracic approach are desirable, for example, by the development of methods to compensate for image degradation caused by the chest wall.

An understanding of ultrasonic aberration produced by the chest wall is important to the development of appropriate compensation methods for transthoracic ultrasonic imaging. Direct measurements of ultrasonic distortion produced by chest wall specimens[7,8] have been helpful. Results reported in Ref. 7 show that propagation through the chest wall causes substantial beam distortion. However, that study did not distinguish the effect of soft tissue from effects caused by rib structures. In Ref. 8, a detailed study of distortion caused by soft tissue paths indicates that soft tissue distortion in the chest wall is substantially less than the corresponding distortion in the human abdominal wall. However, distortion caused by ribs was only treated qualitatively in the latter

[a)]Present address: Department of Meteorology, The Pennsylvania State University, University Park, PA 16802.

study because the physical mechanisms of rib-induced distortion could not be adequately described by the method reported there. Although a model of ultrasound propagation in the chest wall has previously been described,[9] that model is based on coarse depictions of chest wall morphology including homogeneous tissue layers and evenly-spaced, uniformly-shaped ribs. These previous experiments and simulations, therefore, have left gaps in the current knowledge about the physical causes of ultrasonic wavefront distortion caused by the chest wall.

Recent work on the simulation of ultrasonic pulse propagation[10–12] has provided insight about the wavefront distortion caused by the human abdominal wall. Although these studies have provided specific information about the relationships between soft tissue morphology and ultrasonic wavefront distortion, the work is not fully applicable to distortion caused by the human chest wall. The morphology of chest wall soft tissue is different from that of the abdominal wall in ways that can affect ultrasonic wavefront distortion.[8] Furthermore, imaging through the chest wall is complicated by ribs that limit the usable acoustic window size and cause scattering and reflection.

The study reported here applies quantitative simulation methods, similar to those presented in Refs. 10 and 12, to anatomically detailed chest wall models that include the ribs. Accurate depiction of rib–ultrasound interactions requires not only representation of the strong reflections associated with sound speed and density contrast between ribs and soft tissue (already accurately modeled by the finite difference method of Ref. 10), but also modeling of the strong losses associated with propagation through bone and cartilage. For this reason, the finite-difference method described in Ref. 10 has been extended to include tissue-dependent absorption. Quantitative descriptions of the distortion caused by soft tissues are obtained by statistical analysis of simulated distortion. Visualizations of wavefronts propagating through maps of chest cross sections provide evidence about physical relationships between wavefront distortion and the morphology of ribs and soft tissue structures in the chest wall. Further insight about wavefront distortion mechanisms is provided by a comparison of distortion results for incident pulses of different center frequencies.

I. THEORY

Ultrasonic pulse propagation through the human chest wall is modeled here using the equations of motion for a fluid of variable sound speed, density, and absorption. The tissue is assumed motionless except for small acoustic perturbations. Absorption is included using an adaptation of the Maxwell solid model,[13] in which all absorption effects are represented by a single relaxation time. This assumption results in frequency-independent absorption characteristics. Equivalent treatments of tissue-dependent absorption have been employed by a number of previous models for ultrasonic propagation in biological tissues.[14–16] For such a fluid, the linearized equations of mass conservation, momentum conservation, and state can be combined to obtain the first-order, two-dimensional, coupled propagation equations,

$$\frac{\partial p(x,y,t)}{\partial t} + \rho(x,y)\, c(x,y)^2\, \nabla \cdot \mathbf{v}(x,y,t) = -\alpha(x,y)\, p(x,y,t), \tag{1}$$

$$\rho(x,y)\, \frac{\partial \mathbf{v}(x,y,t)}{\partial t} + \nabla p(x,y,t) = 0. \tag{2}$$

Here, $p(x,y,t)$ is the acoustic perturbation in fluid pressure, $\mathbf{v}(x,y,t)$ is the vector acoustic particle velocity, $\rho(x,y)$ is the ambient density, $c(x,y)$ is the ambient sound speed, and $\alpha(x,y)$ is an absorption coefficient that is equivalent to the inverse of a spatially-dependent relaxation time $\tau(x,y)$.

The absorption coefficient α, defined as a real quantity, is related to the energy lost per unit length as follows. The propagation equations (1) and (2) lead, for plane-wave propagation of the form $p = e^{i(kx-\omega t)}$, to the dispersion relation

$$k = \frac{\omega}{c}\, \sqrt{1 + \frac{i\alpha}{\omega}}, \tag{3}$$

where k is the complex wavenumber, ω is the (real) radial frequency $2\pi f$, and c is the (real) sound speed. The imaginary part of the wavenumber k is the absorption in nepers per unit length. Thus, the absorption parameter α can be obtained by a numerical solution of the equation

$$\mathrm{Im}[k] = \frac{\text{loss (dB/length)}}{20 \log_{10}(e)} = \mathrm{Im}\left[\frac{\omega}{c}\sqrt{1 + \frac{i\alpha}{\omega}}\right]. \tag{4}$$

Solution of Eq. (4) results in wavenumbers having a real part that differs from ω/c. Since this discrepancy is less than 1% over the range of tissue properties employed in the present study, use of absorption coefficients computed from Eq. (4) does not significantly affect propagation characteristics except by adding the specified absorption.

Equations (1) and (2) were solved numerically using the finite-difference time-domain (FDTD) method described in Refs. 10 and 17. This method is a two-step MacCormack predictor–corrector algorithm that is fourth-order accurate in space and second-order accurate in time. The computations employed a spatial step size of 15 points per wavelength at the pulse center frequency of 2.3 MHz. Time step sizes were computed using a Courant–Friedrichs–Lewy number of 0.25. Further details on this class of finite difference algorithms can be found in Refs. 18–20.

The initial condition was chosen to model the experimental configuration in Ref. 8, in which a spatially broad, nearly planar wavefront was emitted from a wideband, pulsed, unfocused source far from the tissue layer. The initial wavefront was represented in the present simulation as a plane wave pulse propagating in the $+y$ direction:

$$p(x,y,0) = -\sin[k_0(y-y_0)]\, e^{-(y-y_0)^2/(2\sigma^2)},$$

$$u(x,y,0) = 0,$$

and (5)

$$v(x,y,0) = \frac{p(x,y,0)}{\rho\, c},$$

where the wavenumber k_0 is equal to $2\pi f_0/c$ for a center frequency of f_0, σ is the Gaussian parameter of the pulse temporal envelope, and u and v are the x and y components of the vector acoustic particle velocity **v**. The spatial Gaussian parameter σ was chosen to simulate the bandwidth of the pulse used in the experiments, as discussed below in the Method section.

The computational configuration is analogous to that described in Ref. 10. The domain of computation is two-dimensional, with the y direction taken to be parallel to the direction of propagation and the x direction parallel to the initial wavefront. As in Ref. 10, periodic boundary conditions were applied on the domain edges that were parallel to the direction of propagation, while radiation boundary conditions were applied on the edges perpendicular to the direction of propagation.

II. METHOD

This study employed six chest wall specimens obtained during the autopsies of four different donors between 79 and 85 years of age at death. One specimen (4L) was from a white female, while the others were from white males. After the specimens were obtained, they were stored unfixed at $-20\,^{\circ}\mathrm{C}$ and thawed when needed for study. Wavefront distortion measurements were made on these and other specimens as part of a study described in Ref. 8. In those measurements, 2.3 MHz ultrasonic pulses generated by a 0.5-in. piston transducer propagated through individual chest wall specimens immersed in a $37\,^{\circ}\mathrm{C}$ water bath and the transmitted pulses were measured by a 96-element broadband cardiac array scanned to synthesize a two-dimensional aperture. Statistics describing wavefront distortion, including arrival time fluctuations, energy level fluctuations, and wave shape distortion, were computed for the measured pulses.

For the present study, six of the previously measured specimens were cut into ~7-mm thick cross sections using the technique described in Ref. 10. The slices were then fixed and stained with a modified Gomori's trichrome stain according to the procedure detailed in Ref. 21, so that tissue types could be distinguished. This stain colored muscle tissue red and connective tissue blue while leaving the fat its natural color. Calcified tissue, including bone and cartilage in the current specimens, was not differentially stained by this technique, but the natural contrast between bone, cartilage, and marrow was sufficient to allow tissue mapping. Full-color 300 d.p.i. images of the cross sections were created by placing each stained tissue cross section directly onto the surface of a flatbed digital scanner. Image editing packages (Adobe Photoshop, Version 3.0, and the Gnu Image Manipulation Program, Version 1.0) were used to manually segment the cross sectional images, i.e., to map the images into regions that corresponded to one of six media. The media were water (representing water external to specimens or blood inside blood vessels), fat (including subcutaneous fat, fat interlaced within muscle layers, and marrow), muscle, connective tissue (including skin, septa, and fasciae), cartilage, and bone (including cortical bone and trabeculae within cancellous bone).

The nomenclature employed here for the cross sections corresponds to that of Ref. 8 for the whole specimens from which the cross sections were taken; each cross section is identified by a donor number together with ''L'' or ''R'' to indicate whether the corresponding specimen was taken from the left or right side of the breastplate. Additional numbers were used in Ref. 8 to indicate the intercostal space used in each measurement; here, lower-case letters are used to indicate independent acoustic paths. Wavefront distortion measurement results from four of the specimens employed here (4L, 5L, 7L, and 7R) were reported in Ref. 8. Distortion statistics for specimens 8L and 8R were not presented in Ref. 8 because of limited acoustic windows. No new measurements were made for the present study; statistics describing measured distortion are taken directly from Ref. 8.

The six segmented tissue maps are shown in Fig. 1. All of the cross sections contain a layer of septated subcutaneous fat below the skin. Most of the cross sections also include a layer composed primarily of the major pectoral muscles and their connective fasciae above the ribs. Between the ribs are regions of muscle (internal intercostal and external intercostal groups) interlaced with fat. In some cases, additional thin layers of fat between muscle layers are apparent. Cross sections 4L and 7R are cut along the intercostal spaces parallel to the ribs, so that in each a wide cross section of soft tissue appears. Cross sections 5L, 7L, and 8L are cut perpendicular to the ribs, so that each contains soft-tissue acoustic paths with width equal to the width of the corresponding intercostal spaces. Cross section 8R is cut perpendicular to the sternum at a location of large curvature in the ribs, so that the ribs are diagonally sectioned. Several blood vessels appear in cross sections 4L, 7L, 7R, and 8R; the largest of these is the internal mammary artery.

The basic structure of the cross sections is consistent with standard descriptions of chest wall anatomy.[22,23] Ribs appear in each cross section; each rib is composed of a ''costal cartilage'' near the sternum (shown in most of the cross sections considered here) attached to a ''true rib'' (composed primarily of cancellous bone) at the edge farther from the sternum. In the cross sections considered here, the costal cartilages are primarily composed of calcified cartilage, surrounded by a thin layer of cortical bone (solid, dense bone with microscopic porous structure), which in turn is surrounded by the periosteum, a thin membrane of connective tissue. Cross sections 7L and 7R also appear to contain a small amount of cortical bone in the central portion of the ribs. This phenomenon may be associated with advanced calcification known to occur in aging humans.[24] Cancellous bone, composed of thin trabeculae that form macroscopic cells filled with marrow, is seen in all the ribs of cross section 5L, which was taken at a distance farther from the sternum so that the true ribs, rather than the costal cartilages, were included in this cross section. Some cancellous bone is also apparent within portions of the ribs of cross sections 4L and 8R. In each case, the cancellous bone is surrounded by a thin layer of cortical bone and by the periosteum. A portion of the sternum, composed of cancellous bone surrounded by cortical bone, is visible at the left side of cross section 4L.

The density and sound speed grids needed for the finite-

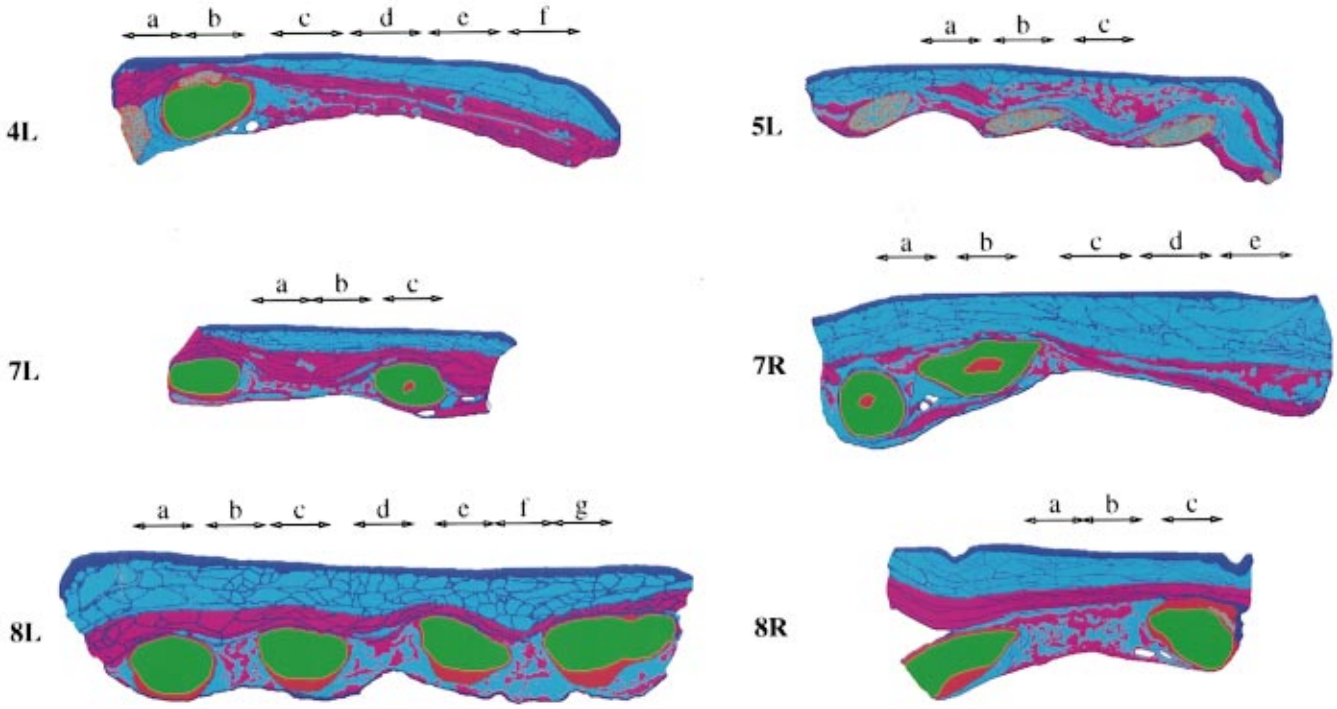

FIG. 1. Chest tissue maps used in simulations. In each map, blue denotes skin and connective tissue, cyan denotes fat, purple denotes muscle, orange denotes bone, and green denotes cartilage. Blood vessels appear as small water-filled (white) regions. Simulated apertures are indicated using lower-case letters for each cross section; the letters correspond to the acoustic path labels used throughout, while the length of the arrow beneath each letter corresponds to the extent of the simulated aperture. Smaller arrows indicate 55-element (11.60-mm) apertures while large arrows indicate 68-element (14.28-mm) apertures.

difference computation were created by mapping regions of the segmented tissue images to reference density and sound speed values for the five tissue types and water. The water sound speed and density employed are those of pure water at body temperature (37.0 °C).[25,26] Sound speeds for muscle and fat were obtained by averaging values for human tissues given in Refs. 27 and 28. A representative sound speed for connective tissue was determined using an empirical formula relating collagen content to ultrasonic sound speed[29] together with a measured value for the collagen content of human skin.[30] The sound speed employed for bone was obtained from an average of values reported in Ref. 31 for longitudinal-wave propagation in human cortical bone. The sound speed used here for cartilage is that given in Ref. 32 as quoted in Ref. 27. Density values for soft tissues were determined from Ref. 33 by averaging values reported for adipose tissue, skeletal muscle, and skin, respectively. Density values employed for bone and cartilage are average values from Ref. 31.

Absorption values were determined from attenuation measurements summarized in Ref. 27 for human fat at 37 °C, human bicep muscle at 37 °C, human skin at 40 °C, human and bovine cartilage at 23 °C, and human skull (temperature not reported). Attenuation values reported at other ultrasonic frequencies were interpolated (or, for the skull data, extrapolated) to obtain values for 2.3 MHz (corresponding to the pulse center frequency employed here and in Ref. 8) assuming a linear dependence of attenuation on frequency. This assumed linear dependence is a simplifying approximation; tissue measurements show that attenuation varies approximately as $\alpha \propto f^{\beta}$, where β is typically between 0.9 and 1.5 for various human soft tissues.[34] The absorption for water was estimated by extrapolating frequency- and temperature-dependent absorption values summarized in Ref. 35 to 2.3 MHz and 37.0 °C. The values of tissue parameters employed in the present study are given in Table I.

The finite-difference program was employed to compute propagation of a plane wave pulse through each scanned cross section from the skin to the peritoneal membrane, mimicking the propagation path employed in the distortion measurements of Ref. 8. The spatial step size of the finite-difference grid was chosen to be 0.0442 mm, or 1/15 wavelength in water at the center frequency of 2.3 MHz. The temporal step size was chosen to be 0.00725 μs, for an optimal Courant–Friedrichs–Lewy number $c\Delta t/\Delta x$ of 0.25.[20] The Gaussian parameter σ of the source pulse was chosen to be 0.4766 mm in accordance with the experimentally measured pulse bandwidth (for pulses transmitted through a water path) of 1.2 MHz. A visual comparison confirmed that the

TABLE I. Assumed physical properties for each tissue type employed in the simulations.

Tissue type	Sound speed (mm/μs)	Density (g/cc)	Absorption (dB/mm)
Water	1.524	0.993	0.0007
Fat	1.478	0.950	0.12
Muscle	1.547	1.050	0.21
Connective	1.613	1.120	0.37
Cartilage	1.665	1.098	0.97
Bone	3.540	1.990	4.37

simulated pulse closely matched the measured pulses in shape and length.

Each simulation was performed on a workstation with 128 MB of random-access memory. Finite-difference grids on the order of 1500×1000 points were employed. At each time step, the wave field was updated on a grid subset chosen to include the entire support of the acoustic wave but to exclude quiescent regions. The entire pressure field was saved as a raster image at intervals of 0.725 μs for later visualization. The computation time for each simulation was on the order of five hours.[36]

Signals were recorded for 8.62 μs at a sampling frequency of 138 MHz by simulated apertures with dimensions close to those in the experimental study of Ref. 8. Positions of all simulated apertures employed are sketched in Fig. 1. The simulation of receiving elements was performed by integrating the locally-computed pressure over the element pitch of 0.21 mm. For cross sections cut parallel to the ribs, the simulated apertures contained 68 elements for an aperture width of 14.28 mm. For cross sections cut perpendicular to the ribs, 55 simulated elements were used to form 11.55 mm apertures. Element directivity effects were implicitly incorporated by the integration of acoustic fields over the width of each element; the resulting directivity functions correspond to those for an idealized line element of width 0.21 mm.

A one-dimensional version of the reference waveform method[10,37] was used to calculate the arrival time of the pulse at each receiving position in the simulation data. In this method, the relative arrival time of each received waveform is computed by cross-correlation with a reference waveform. The arrival time fluctuations across the receiving aperture are then calculated by subtracting a linear fit from these calculated arrival times, and the root-mean-square value of these fluctuations is computed. Energy level fluctuations in the data were calculated by summing the squared amplitudes of each waveform over a 2.4-μs window that isolated the main pulse, converting to decibel units, and subtracting the best linear fit from the resulting values. As for polynomial fits previously employed in wavefront distortion measurements,[8] the purpose of the linear fit removal in each case was to compensate for gross changes in tissue thickness across the array. Variations in pulse shape across the aperture were evaluated using the waveform similarity factor;[37] this quantity, which can be considered a generalized cross-correlation coefficient, has a maximum of unity when all received waveforms are identically shaped.

To test the frequency dependence of chest wall wavefront distortion, propagation through eight portions of specimens, each containing only soft tissue, was also computed for wavefronts having center frequencies of 1.6 and 3.0 MHz. In each case, the initial wavefront was chosen to have the same temporal envelope as above. The absorption coefficient at these frequencies for each tissue type was extrapolated from the value employed at 2.3 MHz using the assumption that absorption depended linearly on the center frequency. The spatial and temporal sampling rates were also varied in inverse proportion to the pulse center frequency. All runs were otherwise identical in configuration and processing to those described above.

TABLE II. Statistics of simulated wavefront distortion caused by thirteen soft tissue paths within chest wall cross sections. The ''Path'' column shows the cross section label and aperture letter for each path; these labels correspond to those shown in Fig. 1. The statistics shown include the average specimen thickness for the tissue path considered, rms values and correlation lengths (CL) of the arrival time fluctuations (ATF) and the energy level fluctuations (ELF), the waveform similarity factor (WSF), and the total attenuation.

		ATF		ELF			
Path	Thickness (mm)	rms (ns)	CL (mm)	rms (dB)	CL (mm)	WSF	Attenuation (dB)
4L-c	15.4	32.0	0.60	1.98	1.68	0.981	5.62
4L-d	12.7	10.0	2.58	0.46	1.23	0.999	4.08
4L-e	16.0	10.0	1.37	1.61	1.74	0.998	5.26
4L-f	17.0	17.3	2.48	0.92	1.61	0.999	5.33
5L-a	11.0	11.6	0.95	1.51	1.13	0.991	4.29
5L-c	15.0	14.8	1.03	1.15	1.19	0.996	5.01
7L-a	16.2	16.8	2.64	0.95	1.29	0.999	5.46
7L-b	14.9	22.5	2.66	1.19	1.61	0.998	4.91
7R-c	17.7	17.4	1.77	2.52	2.07	0.997	5.83
7R-d	21.0	8.3	1.10	0.85	1.79	0.999	7.07
7R-e	24.7	13.7	1.37	1.06	1.62	0.997	8.69
8R-a	23.8	26.6	1.78	2.58	1.40	0.992	7.76
8R-b	22.2	29.9	1.44	1.95	1.11	0.989	6.09
Mean	17.5	17.8	1.67	1.44	1.50	0.995	5.80
St. Dev.	4.2	7.8	0.71	0.66	0.30	0.005	1.33

III. RESULTS

Simulated wavefront distortion results for 13 soft tissue paths (i.e., paths in which wavefront distortion was not significantly influenced by the ribs) are shown in Table II. These results indicate that soft tissue paths cause a wide range of wavefront distortion effects depending on the specific morphology of each path. For instance, path 7R-c causes arrival time and energy level fluctuations that are more than twice the magnitude of those caused by the adjacent path 7R-d. This difference is thought to arise from morphological features, including muscle tissue with interlaced fat and a large amount of connective tissue, of the tissue within path 7R-c. Also notable is that the specimen thickness does not closely correspond to variations in distortion. The largest rms arrival time fluctuation and lowest waveform similarity factor, for example, are caused by path 4L-c, which has an average thickness less than the mean for all the tissue paths.

Wavefront distortion statistics for the 13 soft tissue paths are graphically summarized in Fig. 2 together with corresponding statistics for all of the soft tissue measurements reported in Ref. 8. This comparison indicates that wavefront distortion caused by soft tissues in the chest wall simulations is comparable to measured distortion. Arrival time fluctuations and energy level fluctuations for simulated distortion are slightly less than measured values, but mean values of both fluctuations for the simulations fall well within one standard deviation of the corresponding mean fluctuation for the measurements. The waveform similarity factor, however, is substantially higher for simulations than measurements, indicating that simulated waveforms were distorted considerably less than measured waveforms. Correlation lengths for the simulated distortions are somewhat less

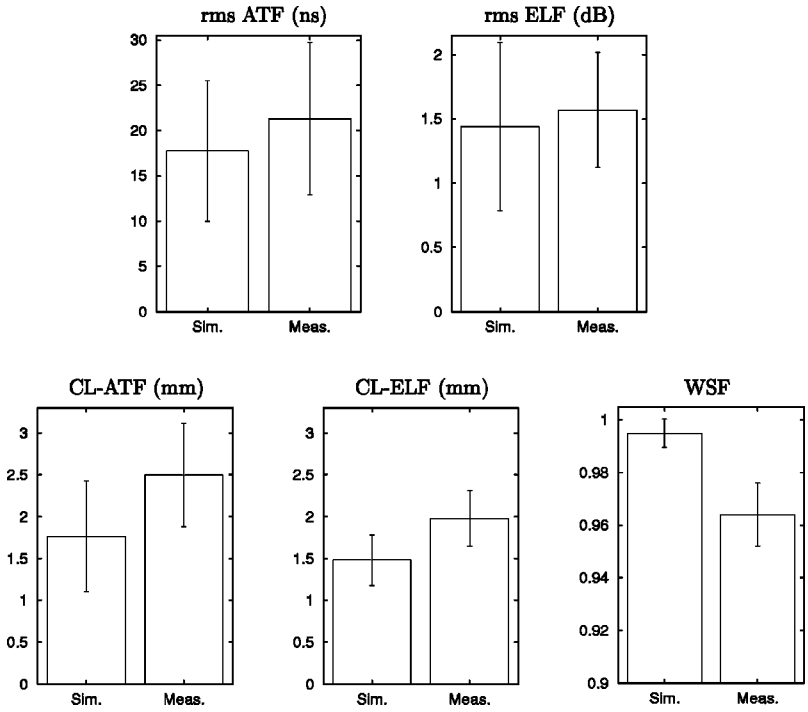

FIG. 2. Summary of distortion statistics for soft tissue paths. The bar chart shows mean values of the rms arrival time fluctuations (ATF), rms energy level fluctuations (ELF), correlation lengths (CL) of these fluctuations, and waveform similarity factors (WSF) for the simulations performed in the present paper and the experiments reported in Ref. 8. Error bars indicate a range of plus or minus one standard deviation from the mean.

than measured values. However, consistent with measurements, the mean correlation length of the simulated arrival time fluctuations is greater than that for the simulated energy level fluctuations.

As in Ref. 8, rib structures were found to cause much more distortion than soft tissue alone. The varied nature of distortion caused by rib effects is illustrated in Fig. 3, which shows three representative sets of measured signals for specimen 8L. These measurements were made during the study reported in Ref. 8. The first panel shows 96 adjacent measured signals, along the array direction (approximately parallel to the ribs) for propagation through a tissue path within an intercostal space. The signals are not severely distorted; secondary arrivals are discernible, but are of lower amplitude than the main arrival. The second panel shows 96 measured signals for an elevation over a rib. Here, all signals are severely distorted. Multiple arrivals, as well as high-amplitude spatially-random fluctuations, are seen. The third panel shows 50 measured signals along the elevation direction (perpendicular to the ribs), centered over the soft tissue between the ribs. Here, the main wavefront is curved rather than straight, an additional arrival behind the main wavefront is seen, and portions of the signals from over the ribs (at both edges of the panel) are advanced relative to the signals from the central soft tissue region.

The present simulations allow more detailed qualitative and quantitative investigation of rib effects than were possible from the previous measurements. Propagation through two rib-influenced paths is illustrated in Figs. 4 and 5, in which computed ultrasonic pulses are superimposed on portions of the tissue maps from Fig. 1. (Similar visualizations of propagation through soft human body wall tissue were shown in Ref. 10.)

Figure 4 shows propagation through a thin rib, composed chiefly of cancellous bone, in cross section 5L (corresponding approximately to path 5L-b). A strong reflection

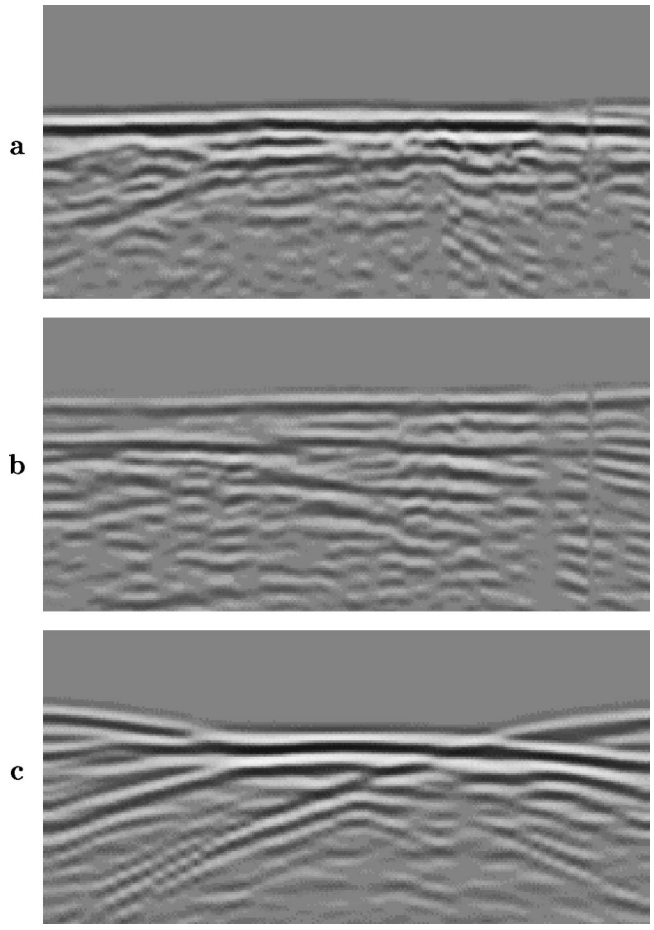

FIG. 3. Measured waveforms for three propagation paths in specimen 8L. Each panel shows received waveforms on a bipolar logarithmic gray scale with a dynamic range of 40 dB. The horizontal range shown in each panel is 20 mm and the vertical range shown is 6.4 μs. (a) Tissue path between two ribs, in azimuth direction (parallel to ribs). (b) Path including a rib, azimuth direction. (c) Tissue path including intercostal space between two ribs, elevation direction (perpendicular to ribs).

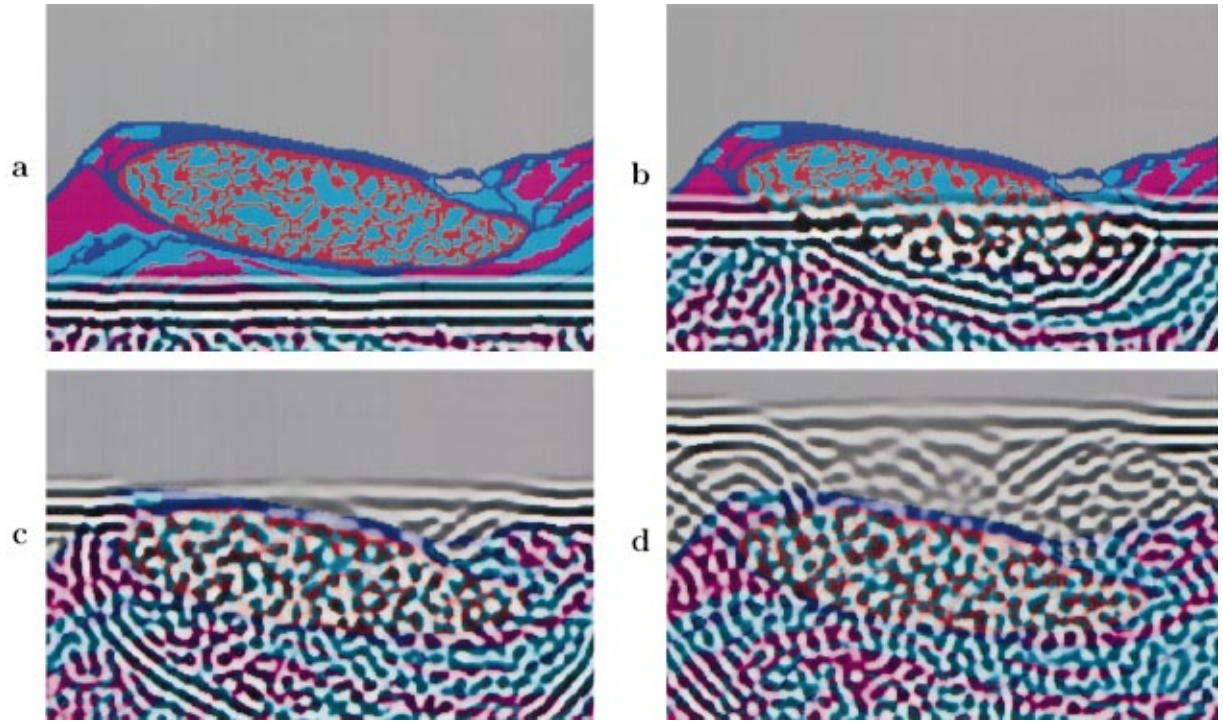

FIG. 4. Simulated propagation through the central rib in cross section 5L (path 5L-b). Panels (a)–(d) show instantaneous acoustic pressure fields at successive intervals of 2.17 μs. Each panel shows an area that spans 20.32 mm horizontally and 14.58 mm vertically. Logarithmically compressed wavefronts are shown on a bipolar scale with black representing minimum pressure, white representing maximum pressure, and a dynamic range of 57 dB.

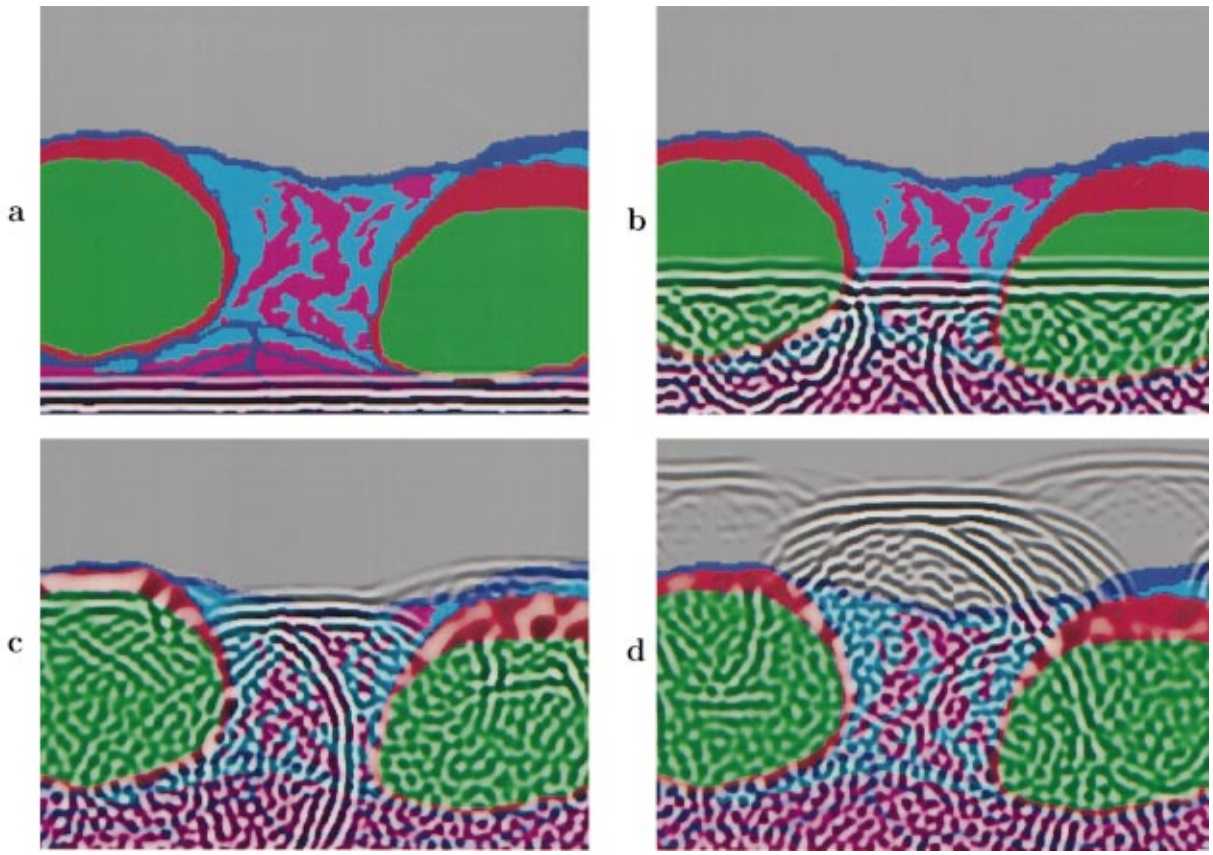

FIG. 5. Simulated propagation through an intercostal space in cross section 8L (path 8L-b). Panels (a)–(d) show instantaneous wavefields at successive intervals of 3.62 μs. Each panel shows an area that spans 28.27 mm horizontally and 21.20 mm vertically. Wavefronts are shown using the same format as in Fig. 4.

occurs at the first interface between bone and soft tissue, removing a substantial amount of energy from the main wavefront. The small, high-contrast trabeculae within the rib cause considerable scattering, as can be observed in panel (b) of Fig. 4. The scattering causes random fluctuations behind the main wavefront; these fluctuations somewhat resemble those seen in the measured data of Fig. 3(b). After passing through the rib, as seen in panels (c) and (d) of Fig. 4, the central portion of the wavefront shows substantial attenuation and distortion. However, the average arrival time of the wavefront is not greatly changed by propagation through the rib, but is advanced by only about one-half period. This phenomenon apparently occurs because the influence of the ''slow'' marrow (modeled here as fat) counteracts the influence of the ''fast'' trabeculae. Noteworthy is that the predominant ultrasonic wavelength has increased after propagation through the rib, so that the effective center frequency of the wavefront has been lowered. Since the absorption model used in the present study includes only frequency-independent absorption, the loss of short-wavelength components in this simulation results only from frequency-dependent scattering caused by the trabeculae.

Propagation within path 8L-b, which includes two larger ribs and the corresponding intercostal space, is illustrated in Fig. 5. At the position of the cross section, these ribs are composed primarily of cartilage and surrounded by a thin layer of cortical bone. Since the cartilage and bone of these ribs are modeled as homogeneous structures, small-scale scattering within these tissues did not occur in this simulation. Instead, the wavefront is reflected from interfaces between cartilage, bone, and soft tissue.

The visualization shown in Fig. 5 provides physical reasons for all the rib-related distortion phenomena seen in the measured data of Fig. 3(c). The wavefronts propagating through the ribs show greater attenuation than that in Fig. 4, both because of the high absorption of the ribs and because of the reflections noted above. These wavefronts are also advanced relative to the wavefront propagating through the intercostal space, because of the higher sound speed of both bone and cartilage. The wavefront propagating through the intercostal space is distorted somewhat by the inhomogeneous soft tissue path, as can be observed in panels (b) and (c). However, much greater distortion results from interaction between the wavefront and the ribs. A rightward-propagating reflection, seen in panels (b) and (c), combines with the main wavefront in panel (d) to result in severe distortion at the right side of the central wavefront. A leftward-propagating reflection from the other rib is also apparent. Furthermore, diffraction from the edges of the ribs results in large curvature of the soft tissue wavefront.

Distortion and attenuation statistics for a variety of simulations employing rib-influenced paths are shown in Table III. Footnotes in Table III indicate physical causes of distortion present within each path. A variety of distortion and attenuation mechanisms are illustrated. Propagation through small intercostal spaces (paths 4L-a, 8L-b, 8L-f, and 7R-a) causes diffraction effects that introduce substantial curvature into the wavefront, as seen in Fig. 5. This large-scale wavefront curvature is associated with large arrival time fluctuation values although the wavefronts generally appear to be locally smooth. Interference between directly-transmitted and rib-reflected wavefronts (paths 4L-a, 8L-b, 8L-d, 8L-f, and 7R-a) introduces arrival time, energy level, and waveform distortion substantially greater than that for soft tissue paths without ribs. Propagation through cancellous bone (paths 4L-a, 4L-b, 5L-b, and 8R-c) results in considerable attenuation and large waveform distortion, while propagation through cortical bone and cartilage (paths 4L-a, 4L-b, 8L-a, 8L-c, 8L-e, 8L-g, 7L-c, 7R-a, 7R-b, and 8R-c) results in even larger attenuation but smaller distortion. Where bone is embedded within cartilage (paths 7L-c and 7R-b), additional scattering also occurs. For the path including a large bone inclusion (path 7R-b), this scattering results in an extremely high energy level and waveform distortion.

TABLE III. Statistics of simulated wavefront distortion caused by fourteen tissue paths including rib structures. The footnotes associated with the label for each path indicate morphological features and physical phenomena that affected the wavefront distortion computed for that path. The format is analogous to that in Table II.

		ATF		ELF			
Path	Thickness (mm)	rms (ns)	CL (mm)	rms (dB)	CL (mm)	WSF	Attenuation (dB)
4L-a[a,b,c,d]	21.0	260.3	3.00	2.58	2.72	0.968	15.33
4L-b[b,c]	17.6	161.9	1.90	4.16	1.49	0.641	43.35
5L-b[b]	14.2	92.5	0.69	3.06	1.92	0.775	26.87
7L-c[c,e]	17.8	47.2	1.58	5.33	2.04	0.958	19.66
7R-a[a,c,d]	30.4	123.1	2.12	3.80	1.78	0.960	16.57
7R-b[c,e]	24.3	165.6	2.71	6.88	2.07	0.274	43.06
8L-a[c]	25.3	113.9	1.18	7.75	2.29	0.907	32.44
8L-b[a,d]	22.8	109.7	2.05	3.43	1.22	0.974	10.28
8L-c[c]	28.8	134.0	2.75	3.04	1.57	0.944	40.47
8L-d[d]	23.6	78.9	0.64	3.06	1.55	0.950	6.78
8L-e[c]	26.4	208.8	1.91	3.62	1.50	0.810	44.27
8L-f[a,d]	28.5	169.9	1.79	5.02	1.95	0.916	10.70
8L-g[c]	27.6	210.8	1.40	3.36	1.35	0.892	44.22
8R-c[b,c]	24.9	81.4	2.08	2.76	1.25	0.962	44.32

[a]Small intercostal spaces.
[b]Cancellous bone.
[c]Cortical bone and cartilage.
[d]Strong rib reflections.
[e]Cortical bone within cartilage.

Computed frequency-dependent wavefront distortion statistics are summarized in Fig. 6. Tissue paths used for these computations, none of which include rib structures, are those labeled 4L-d, 4L-f, 5L-a, 5L-c, 8R-a, 8R-b, 7L-a, and 7L-b in Fig. 1. The results shown in Fig. 6 indicate that arrival time fluctuations, energy level fluctuations, and waveform distortion all become more severe with increasing pulse frequency. The most dramatic change is in the energy level distortion; on average, the rms energy level fluctuations for the 3.0-MHz signals are 2.3 times those for the 1.6-MHz signals. Correlation lengths of both arrival time and energy level fluctuations decrease with frequency, so that the predominant length scales of ultrasonic wavefront distortion are seen to decrease with the ultrasonic wavelength. As with the rms distortion statistics, the most dramatic frequency-dependent change is in the energy level fluctuations. Still, even the high-frequency pulses here show substantially

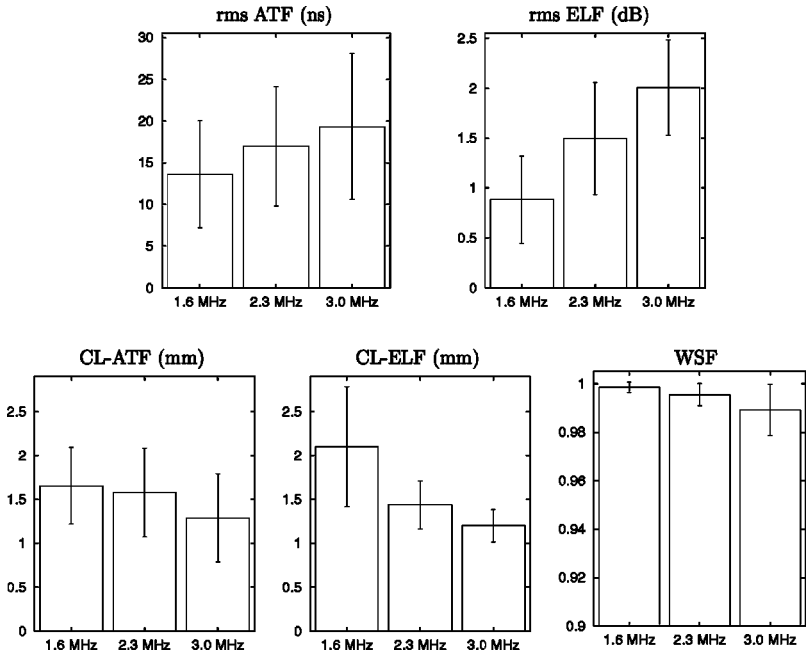

FIG. 6. Summary of simulated frequency-dependent distortion results. Mean rms arrival time fluctuations (ATF), energy level fluctuations (ELF), correlation lengths (CL) of these fluctuations, and waveform similarity factors (WSF) are shown for each of the three pulse frequencies investigated. Error bars indicate a range of plus or minus one standard deviation from the mean.

smaller distortion than that previously observed in experiments and simulations for the human abdominal wall.[10–12,38]

IV. DISCUSSION

As with earlier simulations of propagation through tissue,[10,12] the current study shows qualitative agreement with measured wavefront distortion results for similar specimens.[8] However, the accuracy of the present model is limited by simplifications of true tissue structure. In particular, the computational model here does not account for property variations within tissue types, tissue microstructure, or three-dimensional tissue structure. Each of these simplifications limits the ability of the present model to precisely mimic experimentally measured ultrasonic wavefront distortion. These limitations are discussed, with respect to soft tissues, in Ref. 10.

The modeling of ribs adds additional complication. In the current study, individual trabeculae were assumed to be composed of tissue having properties identical to cortical bone, an assumption known as Wolff's hypothesis.[39] The validity of this hypothesis has been questioned;[40,41] however, measured elastic properties of individual trabeculae vary widely[40,41] and recent work[42] has provided support for Wolff's hypothesis. Thus, the properties employed here for trabecular bone can be regarded as reasonable order-of-magnitude estimates. Likewise, the modeling of marrow as fat tissue is a simplifying assumption that may have limited validity, although available data suggest that the density and sound speed of marrow are close to those for other adipose tissues.[31] In addition, the present model for cartilage is based on measurements of normal cartilage, while the cartilage present in the specimens employed here was calcified due to the age of the donors. However, density measurements made on eight representative samples of calcified cartilage (two from specimen 7R, four from specimen 1R,[8] and two from an unused specimen) resulted in an average density of 0.00111 kg/m^3, which is different by only 1% from the density assumed here. Since sound speed in calcified tissue has been empirically shown to be directly related to density,[43,44] this small change in density suggests that the acoustic properties of the calcified cartilage in our specimens is close to that for normal cartilage.

The computations reported here model the chest wall as a fluid of variable sound speed, density, and compressibility. This model implicitly neglects shear wave propagation. The neglect of shear waves in soft tissues is believed to be justified because the absorption of shear waves in soft tissues is much greater than absorption of longitudinal waves.[45,46] In calcified tissues, however, significant shear waves are known to be generated.[47,48] In the current scattering configuration, some shear waves are likely generated wherever the rib surface is far from parallel to the wavefront. However, since shear wave absorption has been found to be somewhat larger than longitudinal wave absorption for ultrasonic propagation in bone,[47] the significance of shear-wave propagation within bone on transmitted ultrasonic wavefronts is questionable. For this reason, omission of nonlongitudinal waves in the present study, as in another computational study of ultrasonic scattering from bone,[49] is believed to be justified; however, further study would be required to confirm this assumption.

The absence of frequency-dependent absorption is a possible source of error in the present estimates of total tissue attenuation, energy level fluctuations, and waveform distortion. However, since absorption in tissue increases approximately linearly with frequency, lower absorption for frequency components below the pulse center frequency would nearly cancel higher absorption for frequency components above the center frequency, so that the average absorption incurred by a wideband pulse should still be computed with fair accuracy. For this reason, the absence of frequency-dependent absorption in the calculations reported here is not considered to be a significant source of error in the computed attenuation or energy level fluctuation curves. Still, the inclusion of frequency-dependent absorption would result in

additional waveform distortion effects. The lack of this effect is a likely reason for the lower waveform distortion (higher waveform similarity factors) obtained from simulations as compared to measurements. However, the absence of frequency-dependent absorption effects allowed frequency-dependent scattering effects to be clearly quantified separately from absorption effects.

Although the simulations were planned to match the measurements of Ref. 8 closely, a number of differences remain. The most important of these, as discussed in Ref. 10, is that the simulations were performed using a two-dimensional tissue model while the measurements were inherently three-dimensional. Other differences include details of the source waveform and wavefront shape, variations in the specimen orientations and the regions interrogated, and variations in the distance between the specimen and the real or simulated receiving aperture. All of these differences could contribute to discrepancies between measurements and simulations.

In general, most of the simplifying assumptions in the present tissue model are likely to result in underestimation of wavefront distortion produced by the human chest wall. The incorporation of tissue microstructure, spatially-dependent acoustic properties for each tissue type, shear wave propagation in bone and cartilage, three-dimensional propagation, and frequency-dependent absorption could all result in greater spatial and temporal variations in the propagating acoustic fields, so that these features could produce simulated distortion with characteristics closer to measurements. For this reason, distortion statistics computed using the present tissue model should be interpreted as lower limits for the statistics of distortion occurring in real chest wall tissue.

Additionally, some of the discrepancy between simulated and measured distortion may be explained by the nonuniform characteristics of the receiving transducer employed in the measurements.[8] The water-path measurements reported in Ref. 8 show arrival time fluctuations (mean 2.21 ns) and energy level fluctuations (mean 0.36 dB); although small, these fluctuations are comparable to the difference between the average measured and simulated fluctuations. Thus, compensation for arrival time and energy level fluctuations due to transducer irregularities could reduce measured distortion to levels closer to the simulations. Also, the waveform similarity factor for water path measurements was 0.991,[8] which indicates greater waveform distortion than the average value of 0.995 computed here for soft tissue paths. Thus, compensation of the measured data for transducer impulse-response variations could raise the measured waveform similarity factor to a value in closer agreement with simulations.

Previous experimental measurements of wavefront distortion caused by the human chest wall[8] have suggested that distortion caused by chest wall soft tissues is less severe than that caused by the human abdominal wall.[11,38] This difference has been observed to occur even though average specimen thicknesses were comparable in chest wall[8] and abdominal wall[11,38] measurements. The present results provide support for these results; arrival time and energy level distortion by the chest wall was found here to be smaller than that produced by the abdominal wall in previous simulation studies.[10,12] For the simulations, this difference may be partially explained by the fact that the chest wall specimens employed here are thinner on average (mean thickness 17.5 mm) than the abdominal wall cross sections employed in Refs. 10 and 12 (mean thickness 26.7 mm). Another possible partial explanation is that the pulse center frequency employed in abdominal wall measurements and simulations was 3.75 MHz, significantly higher than the center frequency of 2.3 MHz for the chest wall measurements and simulations. Differences in pulse frequency and specimen thickness may explain the discrepancy in energy level distortion between the abdominal wall and chest wall, but do not fully explain the discrepancy in arrival time distortion results. For instance, the mean arrival time and energy level fluctuations per unit length are 1.02 ns/mm and 0.083 dB/mm for the present study vs 1.96 ns/mm and 0.105 dB/mm for the abdominal wall cross sections of Ref. 10 and 12. Arrival time distortion was shown here to increase only subtly with increasing pulse frequency, so that this discrepancy in arrival time fluctuations is not fully explained by pulse frequency differences. However, energy level fluctuations increase markedly with frequency for chest wall tissue. Thus, for equal ultrasonic pulse frequencies, chest wall tissue should cause energy level distortion per unit length comparable to that caused by abdominal wall tissue.

It was suggested in Ref. 8 that chest wall morphology may differ from abdominal morphology in a manner that results in smaller ultrasonic wavefront distortion. The cross sections employed here can be compared with those employed in Refs. 10 and 12 to evaluate the importance of morphological differences between chest wall and abdominal wall tissue. One difference between the two groups of cross sections is the nature of the subcutaneous fat layers. The abdominal wall cross sections generally contain thicker fat layers, containing many more lobular structures than the chest wall cross sections. Since the high contrast between septa and fat causes substantial ultrasonic scattering,[10–12] this morphological difference is likely to result in lower overall energy level and waveform distortion for chest wall tissue (although, as discussed above, the energy level distortion per unit propagation length should be comparable). Also, the abdominal wall and chest wall cross sections have a markedly different structure within the muscle layers that occur below the subcutaneous fat. The abdominal wall cross sections have many large-scale features due to aponeuroses (interfaces between muscle groups, composed of connective tissue and fat) and large fatty regions. These large-scale features cause large wavefront fluctuations that are associated with large rms arrival time fluctuations.[10,12] In contrast, muscle layers of the chest wall cross sections considered here contain primarily smaller-scale structures associated with small islands of interlaced fatty tissue. This morphological difference may result in lower large-scale arrival time fluctuations but significant energy level fluctuations associated with scattering, consistent with the differences between distortion caused by soft tissues in the abdominal wall and the chest wall.

The present results for the frequency dependence of distortion provide further insight into the importance of scatter-

ing effects relative to large-scale structure in wavefront distortion caused by soft tissues. If wavefront distortion in the chest wall were caused only by large-scale tissue structures, the distortion would be roughly independent of frequency, since propagation effects are independent of frequency in the geometric acoustics limit. However, distortion caused by scattering effects should increase with the pulse frequency for inhomogeneities of size comparable to the wavelength. Previous simulation and experimental studies[10–12] on distortion caused by the human abdominal wall have suggested that energy level fluctuations and waveform distortion are generally associated with scattering effects, while arrival time fluctuations are predominantly caused by large-scale path length differences. The present results, while consistent with those conclusions, indicate that scattering plays a role in all types of distortion considered here. Since energy level fluctuations and waveform similarity factors exhibit more dramatic increases in distortion with increasing pulse frequency, the present results suggest that scattering is of primary importance in causing energy level and waveform distortion and of secondary importance in causing arrival time distortion.

These results can be employed to evaluate the potential of various approaches to improve echocardiographic imaging. Available acoustic windows for transthoracic imaging are severely limited by the presence of the ribs, so that image quality cannot be significantly improved by an increase of aperture size. The present results also indicate that use of higher-frequency probes may provide less benefit than expected because of frequency-dependent scattering in the chest wall.

For these reasons, aberration correction methods are potentially important in transthoracic echocardiography, particularly for higher-frequency imaging. The frequency-dependent distortion results reported here suggest that distortion models employing single phase screens may be of some benefit for aberration correction in echocardiography through soft tissue paths. The relatively weak dependence of arrival time fluctuations on pulse frequency suggests that a large portion of arrival time variations are caused by tissue structures too large to cause significant frequency-dependent scattering effects. Similar conclusions regarding the importance of large-scale structures to arrival time fluctuations have also been drawn from results presented in Refs. 10 and 12.

Still, the present results, like those from earlier studies,[10–12] suggest that single phase screens will not provide complete correction for distortion caused by soft tissues. In particular, methods employing single phase screens will not completely remove distortion caused by scattering. The sharp increase of amplitude and waveform distortion with frequency, as well as the moderate increase of arrival time distortion with frequency, indicate that scattering effects become much more important to ultrasonic aberration as imaging frequencies increase. Furthermore, phase screen models do not inherently account for distortion caused by rib structures, shown here to produce diffraction, reflection, and scattering. Thus, any attempted correction using only phase screen models is likely to provide little improvement in the presence of strong rib-induced effects.

Other correction models that incorporate rib structures may provide greater image improvements for the distortions most important to echocardiography. Processing wavefronts with techniques such as angular spectrum filtering can remove some spurious arrivals,[50] although such computations may be difficult to incorporate into a general correction algorithm. Other possible methods include those incorporating models of tissue structure. Models incorporating ray acoustics[9] may provide improvement, but implicitly neglect diffraction and scattering effects, so that aberration correction would be incomplete, particularly for small intercostal spaces. A more complete aberration correction method could employ synthetic focusing using full-wave numerical computation of acoustic fields within sufficiently accurate models of tissue structure. This method has been implemented, within the context of a quantitative frequency-domain inverse scattering method, in Ref. 51. However, the results presented here indicate that distortion caused by soft tissue and rib structures varies widely based on morphological variations between (and within) individuals. Thus, for any general correction method employing models of tissue structure, separate models of tissue structure must be constructed for each region of interest.

V. CONCLUSIONS

A computational study of ultrasonic propagation through the chest wall, including tissue-dependent absorption as well as detailed anatomical cross sections, has been presented. For soft tissue paths, computational results for arrival time distortion, energy level distortion, and correlation lengths of these distortions are comparable to those reported in previous chest wall measurements. Both simulations and measurements indicate that arrival time distortion and energy level distortion caused by soft tissues in the human chest wall is smaller than that caused by the human abdominal wall. Differences in morphology between the abdominal wall and the chest wall provide a probable explanation for this difference.

Distortion caused by rib structures is much more severe than that caused by soft tissues. Reflections and diffraction from rib structures complicate wavefronts that travel through soft tissue paths adjacent to ribs and can cause arrival time and energy level fluctuations much greater than those induced by soft tissue structures. Wavefronts propagating directly through rib structures are attenuated by both internal absorption and reflection at interfaces between bone, cartilage, and soft tissue. Internal scattering within rib structures causes distortion phenomena that include severe waveform and energy level distortion, additional attenuation, and lowering of the effective frequency for the transmitted pulse. The strong dependence of distortion on the morphological details of rib structures presents a major challenge for aberration correction in echocardiography.

Simulation of propagation through soft tissue paths using three different pulse frequencies has indicated that the distortion types investigated here have different frequency dependence. Arrival time fluctuations increase subtly with frequency, while energy level and waveform distortion in-

crease greatly. Thus, a substantial portion of arrival time fluctuations produced by the chest wall may be explained by large-scale tissue variations, but some arrival time distortion and most energy level and waveform distortion apparently result from scattering. Thus, correction of wavefront distortion caused by soft tissues should become both more important and more challenging as pulse frequencies employed in imaging systems are increased.

ACKNOWLEDGMENTS

The authors thank Cari Kelly, Tara Jones, Tracy David, and Michael Pirri for assistance in creating accurate tissue maps of the chest wall cross sections. The original two-dimensional version of the distortion estimation software using the reference waveform method was developed by D.-L. Donald Liu. Funding for this investigation was provided by NIH grants No. DK 45533, No. HL 50855, and No. CA 74050, U.S. Army Grant No. DAMD17-98-1-8141, DARPA Grant N00014-96-0749, and the University of Rochester Diagnostic Ultrasound Research Laboratory Industrial Associates. Some computations were performed at the Cornell National Supercomputing Facility, which was supported in part by the National Science Foundation, New York State, and the IBM Corporation.

[1] H. Feigenbaum, *Echocardiography* (Lea and Febiger, Philadelphia, 1994).
[2] A. E. Weyman, *Principles and Practice of Echocardiography*, 5th ed. (Lea and Febiger, Philadelphia, 1994).
[3] J. T. T. Chen, *Essentials of Cardiac Imaging*, 2nd ed. (Lippincott-Raven, Philadelphia, 1997).
[4] F. M. Clements and N. P. de Bruijn, *Transesophageal Echocardiography* (Little, Brown, and Company, Boston, 1991).
[5] K.-L. Chan, G. I. Cohen, R. A. Sochowski, and M. G. Baird, ''Complications of transesophageal echocardiography in ambulatory adult patients: analysis of 1500 consecutive examinations,'' J. Am. Soc. Echocardiogr. **4**, 577–582 (1991).
[6] W. G. Daniel, R. Erbel, W. Kasper, C. A. Visser, R. Engberding, G. R. Sutherland, E. Grube, P. Hanrath, B. Maisch, K. Dennig, M. Schartl, P. Kremer, C. Angermann, S. Iliceto, J. M. Curtius, and A. Mügge, ''Safety of transesophageal echocardiography: a multicenter survey of 10,419 examination,'' Circulation **83**, 817–821 (1991).
[7] A. D. Savakus, K. K. Shung, and N. B. Miller, ''Distortions of ultrasonic field introduced by the rib cage in echocardiography,'' J. Clin. Ultrasound **10**, 413–419 (1982).
[8] L. M. Hinkelman, T. L. Szabo, and R. C. Waag, ''Measurements of ultrasonic pulse distortion produced by the human chest wall,'' J. Acoust. Soc. Am. **101**, 2365–2373 (1997).
[9] Y. Y. Botros, E. S. Ebbini, and J. L. Volakis, ''Two-step hybrid virtual array-ray (VAR) technique for focusing through the rib cage,'' IEEE Trans. Ultrason. Ferroelectr. Freq. Control **45**, 989–999 (1998).
[10] T. D. Mast, L. M. Hinkelman, M. J. Orr, V. W. Sparrow, and R. C. Waag, ''Simulation of ultrasonic pulse propagation through the abdominal wall,'' J. Acoust. Soc. Am. **102**, 1177–1190 (1997).
[11] L. M. Hinkelman, T. D. Mast, L. A. Metley, and R. C. Waag, ''The effect of abdominal wall morphology on ultrasonic pulse distortion. Part I: Measurements,'' J. Acoust. Soc. Am. **104**, 3635–3649 (1998).
[12] T. D. Mast, L. M. Hinkelman, M. J. Orr, and R. C. Waag, ''The effect of abdominal wall morphology on ultrasonic pulse distortion. Part II: Simulations,'' J. Acoust. Soc. Am. **104**, 3651–3664 (1998).
[13] H. Kolsky, *Stress Waves in Solids* (Clarendon, Oxford, UK, 1953), pp. 106–129.
[14] S. Leeman, L. Hutchins, and J. P. Jones, ''Bounded pulse propagation,'' in *Acoustical Imaging*, edited by P. Alais and A. F. Metherell (Plenum, New York, 1982), Vol. 10, pp. 427–435.
[15] S. Finette, ''Computational methods for simulating ultrasound scattering in soft tissue,'' IEEE Trans. Ultrason. Ferroelectr. Freq. Control **34**, 283–292 (1987).
[16] C. W. Manry and S. L. Broschat, ''FDTD simulations for ultrasound propagation in a 2-D breast model,'' Ultrason. Imaging **118**, 25–34 (1996).
[17] V. W. Sparrow and R. Raspet, ''A numerical method for general finite amplitude wave propagation and its application to spark pulses,'' J. Acoust. Soc. Am. **90**, 2683–2691 (1991).
[18] R. W. MacCormack, *Lecture Notes in Physics* (Springer-Verlag, Berlin, 1971), Vol. 8, p. 151.
[19] D. Gottlieb and A. Turkel, ''Dissipative two-four methods for time-dependent problems,'' Math. Comput. **30**, 703–723 (1976).
[20] E. Turkel, ''On the practical use of high-order methods for hyperbolic systems,'' J. Comput. Phys. **35**, 319–340 (1980).
[21] L. M. Hinkelman, L. A. Metlay, C. J. Churukian, and R. C. Waag, ''Modified Gomori trichrome stain for macroscopic tissue slices,'' J. Histotech. **19**, 321–323 (1996).
[22] H. Gray, *Gray's Anatomy*, edited by T. P. Pick and R. Howden (Gramercy, New York, 1977), pp. 358–364 (facsimile of 1901 American edition of *Anatomy, Descriptive and Surgical*).
[23] R. Warwick and P. L. Williams, *Gray's Anatomy*, 35th ed. (Saunders, Philadelphia, 1973), pp. 488–490, 519–527.
[24] A. Elkeles, ''Sex differences in the calcification of the costal cartilages,'' J. Am. Geriat. Soc. **14**, 456–461 (1966).
[25] N. Bilaniuk and G. S. K. Wong, ''Speed of sound in pure water as a function of temperature,'' J. Acoust. Soc. Am. **93**, 1609–1612 (1993).
[26] *Handbook of Chemistry and Physics*, edited by R. C. Weast (CRC Press, Boca Raton, 1985), p. F-10.
[27] S. A. Goss, R. L. Johnston, and F. Dunn, ''Comprehensive compilation of empirical ultrasonic properties of mammalian tissues,'' J. Acoust. Soc. Am. **64**, 423–457 (1978).
[28] S. A. Goss, R. L. Johnston, and F. Dunn, ''Compilation of empirical ultrasonic properties of mammalian tissues II,'' J. Acoust. Soc. Am. **68**, 93–108 (1980).
[29] J. E. Olerud, W. O'Brien, M. A. Riederer-Henderson, D. Steiger, F. K. Forster, C. Daly, D. J. Ketterer, and G. F. Odland, ''Ultrasonic assessment of skin and wounds with the scanning laser acoustic microscope,'' J. Invest. Dermatol. **8**, 615–623 (1987).
[30] R. E. Neuman and M. A. Logan, ''The determination of collagen and elastin in tissues,'' J. Biol. Chem. **186**, 549–556 (1950).
[31] F. A. Duck, *Physical Properties of Tissue: A Comprehensive Reference Book* (Academic, New York, 1990).
[32] K. T. Dussik and D. J. Fritch, ''Determination of sound attenuation and sound velocity in the structure constituting the joints, and of the ultrasonic field distribution within the joints on living tissues and anatomical preparations, both in normal and pathological conditions,'' Progress Report to Public Health Service, National Institutes of Health Project A454, 15 September 1956.
[33] H. Q. Woodard and D. R. White, ''The composition of body tissues'' Br. J. Radiol. **59**, 1209–1219 (1986).
[34] International Commission on Radiation Units and Measurements, *ICRU Report 61: Tissue Substitutes, Phantoms, and Computational Modelling in Medical Ultrasound* (ICRU, Bethesda, MD, 1998), pp. 43–51.
[35] K. H. Herzfeld and T. A. Litovitz, *Absorption and Dispersion of Ultrasonic Waves* (Academic, New York, 1959), pp. 353–361.
[36] Simulations were performed on a Linux workstation with an AMD K6 processor running at 200 MHz and 128 MB of random-access memory. The simulation code was written in Fortran 77 and compiled using the front end fort77 and the Fortran-to-C converter f2c with the Gnu C compiler gcc.
[37] D.-L. Liu and R. C. Waag, ''Correction of ultrasonic wavefront distortion using backpropagation and a reference waveform method for time-shift compensation,'' J. Acoust. Soc. Am. **96**, 649–660 (1994).
[38] L. M. Hinkelman, D.-L. Liu, L. A. Metlay, and R. C. Waag, ''Measurements of ultrasonic pulse arrival time and energy level variations produced by propagation through abdominal wall,'' J. Acoust. Soc. Am. **95**, 530–541 (1994).
[39] J. Wolff, *Das Gesetz der Transformation der Knochen* (Hirschwald, Berlin, 1982).
[40] J. C. Rice, S. C. Cowin, and J. A. Bowman, ''On the dependence of the elasticity and strength of cancellous bone on apparent density,'' J. Biomech. **21**, 155–168 (1988).
[41] J. Y. Rho, R. B. Ashman, and C. H. Turner, ''Young's modulus of trabecular and cortical bone material: ultrasonic and tensile measurements,'' J. Biomech. **26**, 111–119 (1993).
[42] C. H. Turner, J. Rho, Y. Takano, T. Y. Tsui, and G. M. Pharr, ''The

elastic properties of trabecular and cortical bone tissues are similar: results from two microscopic measurement techniques,'' J. Biomech. **32**, 437–441 (1999).
[43] S. Lees, J. M. Ahern, and M. Leonard, ''Parameters influencing the sonic velocity in compact calcified tissues of various species,'' J. Acoust. Soc. Am. **74**, 28–33 (1983).
[44] S. Lees, ''Sonic properties of mineralized tissues,'' in *Tissue Characterization with Ultrasound*, edited by J. F. Greenleaf (CRC Press, Boca Raton, 1986), pp. 207–226.
[45] L. A. Frizzell, E. L. Carstensen, and J. F. Dyro, ''Shear properties of mammalian tissues at low MHz frequencies,'' J. Acoust. Soc. Am. **60**, 1409–1411 (1976).
[46] E. L. Madsen, H. J. Sathoff, and J. A. Zagzebski, ''Ultrasonic shear wave properties of soft tissues and tissuelike materials,'' J. Acoust. Soc. Am. **74**, 1346–1355 (1983).
[47] L. Adler and K. V. Cook, ''Ultrasonic properties of freshly frozen dog tibia,'' J. Acoust. Soc. Am. **58**, 1107–1108 (1975).
[48] S. S. Kohles, J. R. Bowers, A. C. Vailas, and R. Vanderby, ''Ultrasonic wave velocity measurement in small polymeric and cortical bone specimens,'' J. Biomech. Eng. **119**, 232–236 (1997).
[49] K. Chandra and C. Thompson, ''Ultrasonic characterization of fractal media,'' Proc. IEEE **81**, 1523–1533 (1993).
[50] L. M. Hinkelman and D.-L. Liu, ''Measurement and analysis of ultrasonic pulse wavefront distortion produced by chest wall,'' *Proceedings of the 12th Annual University of Rochester Diagnostic Ultrasound Research Laboratory Industrial Associates Meeting*, 1995, pp. 8–25.
[51] T. D. Mast, A. I. Nachman, and R. C. Waag, ''Focusing and imaging using eigenfunctions of the scattering operator,'' J. Acoust. Soc. Am. **102**, 715–725 (1997).